Chemical routes to materials

Synthesis of Rh nanoparticles in alcohols: magnetic and electrocatalytic properties

E. Ramírez-Meneses[1,*] , K. Philippot[2,3] , M. A. Domínguez-Crespo[4] , M. Ibrahim[2,3] ,
I. Betancourt[5] , A. M. Torres-Huerta[4] , and A. Ezeta-Mejia[6]

[1] Departamento de Ingeniería Química, Industrial y de Alimentos, Universidad Iberoamericana, Prolongación Paseo de la Reforma 880, Lomas de Santa Fe, C.P. 01219 Ciudad de México, Mexico

[2] LCC (Laboratoire de Chimie de Coordination), CNRS, 205 Route de Narbonne, BP 44099, 31077 Toulouse Cedex 4, France

[3] Université de Toulouse, UPS, INPT, 31077 Toulouse Cedex 4, France

[4] Instituto Politécnico Nacional, Centro de Investigación en Ciencia Aplicada y Tecnología Avanzada - Unidad Altamira, Km 14.5 Carretera Tampico-Puerto Industrial, C.P. 89600 Altamira, Tamaulipas, Mexico

[5] Departamento de Materiales Metálicos y Cerámicos, Instituto de Investigaciones en Materiales, Universidad Nacional Autónoma de México, C.P. 04510 Ciudad de México, Mexico

[6] Instituto Politécnico Nacional, Escuela Superior de Ingeniería Química e Industrias Extractivas, UPALM Ed. 7, C.P. 07738 Zacatenco, Ciudad de México, Mexico

ABSTRACT

The synthesis of Rh nanoparticles has been performed through an organometallic approach starting from the tris(allyl) rhodium complex, $Rh(\eta^3\text{-}C_3H_5)_3$, as precursor and using an alcohol as both a solvent and a stabilizer, under mild reaction conditions (room temperature; 3 bar H_2). The influence of the alcohol used, among methanol, propanol or heptanol, on the morphological and structural characteristics as well as on the magnetic and electrocatalytic properties of the obtained Rh nanoparticles has been investigated. Assemblies of Rh nanoparticles of various sizes have been observed depending on the alkyl chain length of the alcohol used. A noticeable effect of the nanostructured character of these Rh nanoparticles is the appearance of a ferromagnetic ordering at room temperature due to a modified electronic structure. Magnetic moments per atom were determined as follows: 0.099, 0.073 and 0.036 μ_B for methanol, heptanol and propanol, respectively. The electrochemical evaluation of these Rh nanoparticles on the oxygen reduction reaction (ORR) showed that the electroactivity depends on the chain length of the alcohol; thus, Rh-heptanol system displayed the highest electroactivity for ORR.

Address correspondence to E-mail: esther.ramirez@ibero.mx

Springer

Introduction

Fuel cells are widely recognized as very promising devices to obtain electric power directly from the combustion of chemical compounds. Fuel cells are also advantageous because they release less, if any, harmful emissions during operation and, in some cases, the fuel used to power fuel cells can be considered renewable [1]. An interesting family of fuel cells is the one based on polymer proton-conducting membranes (polymer electrolyte membrane fuel cells, PEMFCs) [2], due to low operating temperatures and versatility of applications. To accelerate the desired redox reactions occurring at both the anode and cathode of a PEMFC, a catalyst is required. Currently, the most active electrocatalyst toward both the hydrogen oxidation reaction (HOR) and oxygen reduction reaction (ORR) is Pt (and its alloys) [3]. Since the ORR is about 5 orders of magnitude slower than the HOR, the cathode of a PEMFC typically contains 80–90% of the total Pt in the PEMFC [4]. Unfortunately, even when deposited as nanoparticles, the high cost of Pt has been one of the major barriers to the widespread commercialization of PEMFCs [5]. For these reasons, there has been significant interest in developing other noble metal catalysts to reduce or completely eliminate the use of Pt in PEMFCs.

Noble metal nanoparticles have been synthesized by top-down and bottom-up methods with controlled morphology and size. Bottom-up methods generally involve reducing metal ions to metal atoms, followed by their controlled aggregation in the presence of stabilizers [6–10]. Once selected the method to obtain metal nanoparticles, their organization into two-dimensional structures may be important for some applications. Self-assembly has been demonstrated to be an efficient approach for spontaneous generation of ordered structures using nanoparticles as building blocks [11–13]. Currently, nanoparticle assemblies can be prepared by different strategies that integrate both synthesis and assembly into one step.

The development of new materials with catalytic properties for oxygen reduction reaction is presently a challenge of great technological importance. Ruthenium, osmium- and rhodium-based materials have proved to accomplish the ORR in acidic media [14–16] and hence can be considered as an alternative metal for as catalysts in PEMFCs.

Compared to other noble metal nanoparticles, there are only a few papers dealing with the elaboration of Rh nanoparticles. Table 1 shows a brief overview of previously reported syntheses of Rh nanoparticles. The most notably approach is based on the chemical reduction of $RhCl_3$ as rhodium source and the use of polymers or surfactants to stabilize the obtained Rh nanoparticles in relatively mild reaction conditions [17–20]. Some examples report the use of other stabilizers [21–23] or no stabilizer [24–26]. Alternative precursors, such as Na_3RhCl_6, $(NH_4)_3$ $RhCl_6$, $[(C_5H_{11}CO_2)_2Rh]_2$ and $[Rh(O_2CC_7H_{15})_2]_2$, have been also employed [27–31]. However, the use of organometallic precursors like $Rh_6(CO)_{16}$, $Rh(CO)_2$ (acac), $[Rh(\mu\text{-}OMe)(cod)]_2$, $Rh(acac)(1,5\text{-}C_8H_{12})$, $[Rh(\mu\text{-}Cl)(1,5\text{-}cod)]_2$ and $Rh(\eta^3\text{-}C_3H_5)_3$ is quite rare [32–40]. Other interesting strategies related to the preparation of rhodium nanoparticles take advantages of using templates to direct the particle growth [26, 32].

One main objective when synthesizing new nanomaterials for electrocatalysis is to have at disposal well-controlled materials in terms of size, shape and dispersion of the particles but also to have a good control of their surface properties and deposition on the working electrode. All these parameters are of high importance in order to improve their catalytic performance [41–46]. As it will be described later into detail, the synthesis of Rh nanoparticles was carried out from the $Rh(\eta^3\text{-}C_3H_5)_3$ complex to take advantage of the organometallic approach which is known to allow the formation of small nanoparticles with a clean metal surface. Different alcohols, namely methanol $CH_3\text{-}OH$, propanol $C_3H_7\text{-}OH$ or heptanol $C_7H_{15}\text{-}OH$, were used as both reaction medium (solvent) and stabilizer, in order to determine fitting conditions for ORR activity in PEMFC. Changes in the carbon-supported self-assembly Rh nanoparticles and their influence on the corresponding ORR activities are discussed in terms of the chemical affinity. To our best knowledge, this work is the first report that describes the use of $Rh(\eta^3\text{-}C_3H_5)_3$ complex to synthesize Rh nanoparticles in view of their application in electrocatalysis. Therefore, it opens the way for the investigation of other materials of this nature for this domain of application.

Table 1 Overview of some reported methods for the synthesis of Rh nanoparticles

Synthesis method	Metal precursors	Reducing agents	Stabilizer	Particle size (nm)	References
Chemical reduction of metal salts	$RhCl_3$	$NaBH_4$	N,N-dimethyl-N-cetyl-N-(2-hydroxyethyl) ammonium salts	∼ 3	[17]
Chemical reduction of metal salts	$RhCl_3 \cdot 3H_2O$	$NaBH_4$	New self-assembled supramolecular complexes of cyclodextrins and surfactants	1.2–1.5	[18]
Chemical reduction of metal salts	$RhCl_3$	$NaBH_4$	Polyvinylpyrrolidone (PVP)	∼ 30	[19]
Modified polyol method	$RhCl_3$	Ethylene glycol	Polyvinylpyrrolidone	7–14	[20]
Chemical reduction of metal salts	$RhCl_3$	$[LiB(C_2H_5)_3H]$	$CH_3(CH_2)_{11}$-SH	1–3	[21]
Chemical reduction of metal salts in alcoholic media	$RhCl_3 \cdot xH_2O$	Ethylene glycol	Sodium citrate	3	[22]
Chemical reduction of metal salts	$RhCl_3 \cdot 3H_2O$	Sodium(2-(diphenylphosphino) ethyl) phosphonate	–	∼ 2.3	[23]
Modified pulse microwave-assisted polyol	$RhCl_3$	Ethylene glycol	–	∼ 3	[24]
Salt-templated	$RhCl_3 \cdot 3H_2O$	Sodium oleate	–	∼ 1.6 nm	[25]
Chemical reduction of metal salt	$RhCl_3 \cdot 3H_2O$	$(CH_3)_2NH \cdot BH_3$	Laurate anion (dodecanoate)	5.2 ± 2.7	[23]
Reverse micelle	$Na_3RhCl_6 \cdot 12H_2O$	$NaBH_4$	Dodecanethiol	1.5–3	[27]
Solvothermal	$Rh_6(CO)_{16}$	–	–	20–40	[29]
Thermolysis	$Rh_6(CO)_{16}$	–	–	Not indicate	[30]
Chemical vapor deposition	$Rh(CO)_2(acac)$	–	–	2–3 nm	[31]
Soft micelle template	$(NH_4)_3RhCl_6$	$NaBH_4$	Cetyltrimethylammonium bromide, CTAB	1–2 nm	[26]
One-pot strategy	Na_3RhCl_6	Triethylene glycol	Ascorbic acid/citric acid	∼ 18	[28]
Synthesis in situ dehydrogenation of $(CH_3)_2NH \cdot BH_3$	$[(C_5H_{11}CO_2)_2Rh]_2$	$(CH_3)_2NH \cdot BH_3$	Dimethylammonium hexanoate	1.6–2.3	[30]
One-pot synthesis	$[Rh(O_2CC_7H_{15})_2]_2$	*Tert*-butylamine-borane	*Tert*-butylammonium octanoate	2 ± 0.5	[31]
One-step synthesis	$[Rh(\mu-Cl)(1,5-cod)]_2$	$N_2H_4BH_3$	Amorphous polyaminoboranes $[BNRH_x]_y$ acting as a support	2.7 ± 0.6	[40]
Organometallic approach	$Rh(\eta^3-C_3H_5)_3$	Dihydrogen	PVP	∼ 2	[34, 35]
Organometallic approach	$Rh(\eta^3-C_3H_5)_3$	Dihydrogen	Triphenylphosphine, or 1,4-bis(diphenyl) phosphinobutane	1.3–1.7	[36]
Organometallic approach	$Rh(\eta^3-C_3H_5)_3$ or $[Rh(\mu-OMe)(cod)]_2$	Dihydrogen	Chiral diphosphite ligands	1.9–2.8	[32]
Organometallic approach	$Rh(acac)(1,5-C_8H_{12})$	Dihydrogen	PVP, hexadecylamine	15–50	[33]

Experimental section

Precursor preparation and synthesis of Rh Nanoparticles

The Rh source, $Rh(\eta^3\text{-}C_3H_5)_3$, was prepared according to process elsewhere reported [47–49], from rhodium(III) chloride tri-hydrate, $RhCl_3 \cdot 3H_2O$ (Johnson Matthey) and allyl magnesium chloride, ($H_2C=CHCH_2MgCl$), (Sigma-Aldrich; solution 2.0 M in THF).

The synthesis of Rh nanoparticles was easily carried out by decomposition of $Rh(\eta^3\text{-}C_3H_5)_3$ under

operation allowed to get a dry and black sample of Rh nanoparticles in each case.

A similar procedure was followed to obtain hexadecylamine (HDA)-stabilized Rh nanoparticles. $Rh(\eta^3\text{-}C_3H_5)_3$ (0.663 mmol) was introduced in a Fisher–Porter bottle under argon atmosphere and dissolved in tetrahydrofuran, THF (150 mL, 99%, Sigma-Aldrich), as a solvent in the presence of HDA (0.36 mmol HDA, 98%, Sigma-Aldrich) as a stabilizer. In this last case, no alcohol was used, the amine being the stabilizing agent.

The representative synthesis of alcohol-stabilized-Rh nanoparticles is shown as follows.

$$(1)$$
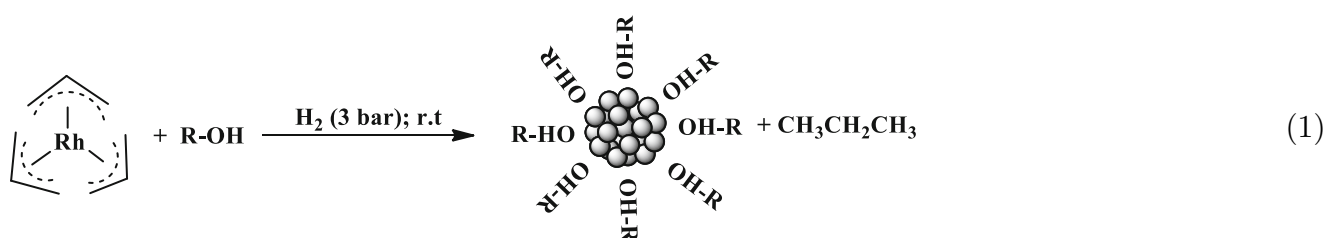
hydrogen pressure and at room temperature in a Fisher–Porter bottle following previous reports by Philippot et al. [37–39]. Three different alcohols were employed, namely methanol (CH_3–OH, 98.9%, Sigma-Aldrich), propanol (C_3H_7–OH, 99.5%, Sigma-Aldrich) and heptanol (C_7H_{15}–OH, 99.5%, Sigma-Aldrich) in order to study the influence of the alkyl chain length on the particle size and on the electrochemical behavior of these catalysts according to a simple standard procedure as follows: $Rh(\eta^3\text{-}C_3H_5)_3$ (0.663 mmol) was introduced in a Fisher–Porter bottle under argon atmosphere. Thereafter, CH_3–OH (150 mL), C_3H_7–OH (150 mL) or C_7H_{15}–OH (150 mL) was added in the reactor leading to a yellow solution. Then, the reactor was pressurized with 3 bar hydrogen (99.999 purity, Alphagaz) at room temperature under vigorous stirring. A color change of the solution from yellow to black was rapidly observed. The reaction mixture was left under vigorous stirring overnight (ca. 16 h) to assure the total decomposition of the Rh precursor. After this period of time, a homogeneous dark brown colloidal solution was formed in all cases. Each colloidal dispersion was then evaporated under vacuum to eliminate the propane formed after hydrogenation of the Rh precursor ligands as well as the excess alcohol. This

where R–OH: methanol, CH_3OH; propanol, C_3H_7OH; heptanol, $C_7H_{15}OH$

To determine the dispersion and particle size of each Rh system, specimens for analysis by transmission electron microscopy (TEM) were prepared by depositing a drop of each crude colloidal solution onto a carbon-coated copper grid. TEM observations were performed on a JEOL 1011 electron microscope, operating at 100 kV with resolution point of 4.5 Å. X-ray diffraction (powder-XRD) patterns were collected in a D2 Phaser Bruker diffractometer coupled to a copper anode in X-ray tube in Bragg–Brentano theta–theta configuration. TOPAS 5 software was used to perform Rietveld refinements where a fundamental parameter model was selected to describe diffractometer contribution [50]. Rhodium crystallographic information was taken as starting model according to the previous report by Lejaeghere et al. [51]. The considered range in 2-theta was from 35° to 90° with a step size of 0.01° and 10 s of collection time/step by a 1-D detector.

Catalyst preparation

The electrochemical activity of the electrode materials was performed using glassy carbon rod as an electrode support (5.0 mm in diameter). The base of the

rod was polished with a cloth and alumina powder (ca. 0.3 μm). 2.0 ± 0.03 mg of carbon-supported Rh nanoparticles sample (Vulcan carbon black + Rh nanoparticles, 4:1 ratio) was dispersed in 10 μL Nafion® and 1 mL ethanol, and then the mixture was sonicated for 30 min to get an uniform suspension or homogeneous catalyst "ink." Thereafter, the glassy carbon electrode was coated with 5 μL of the obtained suspension and dried at room temperature. The nominal loading of Rh nanoparticles was 0.0092 ± 0.0002 mg cm^{-2}. The electrodes were carefully prepared in order to obtain reproducible electrode surfaces and comparable electrocatalytic results.

Electrochemical measurements

Rotating disk electrode (RDE) half-cell testing was performed to study the oxygen reduction reaction (ORR) activity of the rhodium nanostructured catalysts. A PAR Bistat connected to a model 636 RDE setup was used for the testing. The half-cell solution used was oxygen-saturated 0.5 M H_2SO_4. The electrochemistry measurements were taken in a conventional three-electrode arrangement. An Ag/AgCl(sat KCl) reference electrode and a Pt wire counter electrode were used in the system. All potentials reported in this work are referenced *versus* the standard hydrogen electrode (SHE). RDE activity was verified using the Koutecky–Levich equation and the method described for ORR activity testing.

$$\frac{1}{j} = \frac{1}{j_k} + \frac{1}{B\omega^{0.5}} \tag{2}$$

$$B = 0.62\, nF\, Co_2(Do_2)^{2/3} v^{1/8} \tag{3}$$

where j is the current density (A cm^{-2}), j_k is the kinetically controlled current density, n is the number of electrons transferred per molecule of oxygen, F is the Faraday constant, Co_2 is the O_2 concentration in the electrolyte (1.1 E-6 mol cm^{-3} [25, 26]), Do_2 is the diffusion coefficient for molecular oxygen in 0.5 M H_2SO_4 at 25 °C (1.4 E-5 cm^2 s^{-1} [52–54]), and v is the kinematic viscosity of the 0.5 M H_2SO_4 solution at 25 °C (0.01 cm^2 s^{-1} [55]). The angular rotation rate in radians per second is represented as ω. A series of cyclic voltammograms were acquired at 20 mV s^{-1} from − 0.3 to 1.0 V versus Ag/AgCl. All the specimens were analyzed until 50 cyclic potential scans in order to produce clean surfaces. The steady-state polarization curves were recorded in the range from

0.0 to 0.7 V versus Ag/AgCl using a scan rate of 5 mV s^{-1} at 100, 200, 400, 800, 1600 rpm. The number of electrons transferred per oxygen molecule (n) was determined from the slope of the linear relation of $1/j$ and $1/\omega^{1/2}$. Once the kinetic current was extracted; the j_k versus E data were plotted in the typical fuel cell performance style. The resistance losses were extracted from the slope of the linear region of the j_k versus E plot.

Magnetic measurements

Magnetic measurements for Rh nanoparticles were taken in a Magnetic Property Measurement System (MPMS) at room temperature with a maximum applied field of 30,000 Oe. Separations of paramagnetic and ferromagnetic contributions were carried out by fitting the Brillouin function.

$$M = M_0 \left[\frac{2J+1}{2J} \mathrm{Coth}\ \left(\frac{2J+1}{2J}x\right) - \frac{1}{2J}\mathrm{Coth}\left(\frac{x}{2J}\right) \right] \tag{4}$$

where M_0 corresponds to the saturation of the paramagnetic state, J the total angular momentum and $x = \frac{gJ\mu_B H}{k_B T}$ (with g the Landau factor, μ_B the Bohr magneton, H the external magnetic field, k_B the Boltzmann constant, and T the absolute temperature). By considering the experimental magnetization M as the sum of paramagnetic M_{param} and ferromagnetic M_{ferro} contributions ($M = M_{\mathrm{param}} + M_{\mathrm{ferro}}$), the ferromagnetic part was calculated as the subtraction $M - M_{\mathrm{param}}$ [56]. Fitting of experimental data with Eq. (4) uses M_0 and J as adjustable parameters.

Results and discussion

Structural and morphological characterization

The morphology of the as-synthesized rhodium nanoparticles has been studied by electron transmission microscopy (TEM) analysis. Figure 1 presents the TEM and HRTEM images recorded for each sample of Rh nanoparticles as a function of the alcohol used for their synthesis: methanol, propanol and heptanol. HRTEM images of Rh nanoparticles stabilized with hexadecylamine in THF are also shown as a reference, as shown in Fig. 1. For all the alcohol-stabilized Rh nanoparticles, it can be

Figure 1 TEM images of Rh nanoparticles synthesized by hydrogenation of Rh(η^3-C$_3$H$_5$)$_3$ in methanol, propanol, heptanol and HDA/THF.
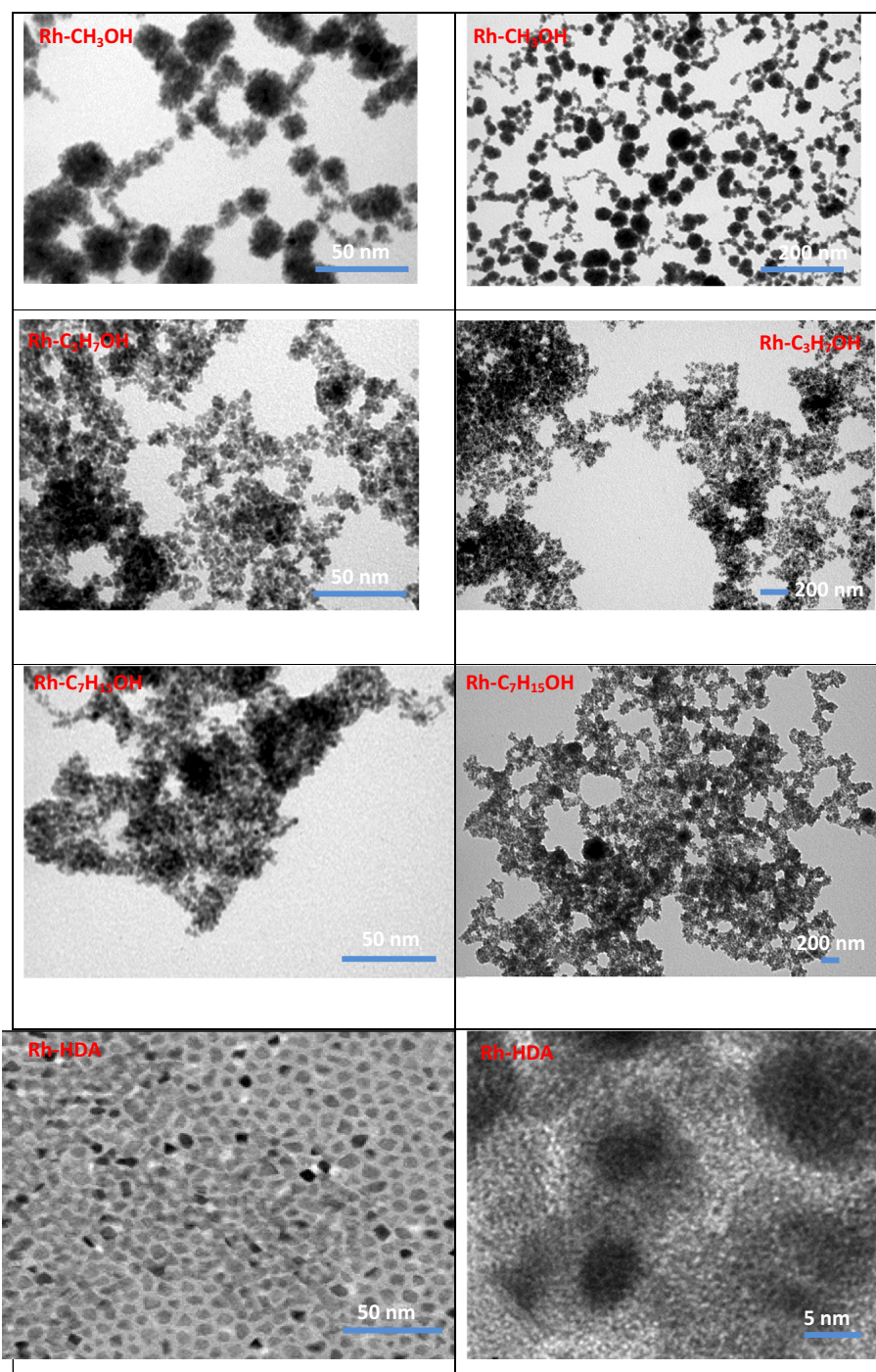
observed the presence of small nanoparticles forming agglomerates with a sponge-like structure. The agglomerates observed for the methanol-stabilized Rh nanoparticles are dark and display a quite large size distribution in the range 15–35 nm, i.e., chain-like assembles of smaller nanoparticles are also visible. The agglomerates observed with Rh nanoparticles prepared by using propanol and heptanol appear more regular in size being in the range 10–50 nm. Similar agglomerates of individual nanoparticles have been previously observed with ruthenium (prepared by decomposition of Ru(1,5-cyclooctadiene)(1,3,5-cyclooctatriene) complex under H$_2$ in a pure alcohol), also with an influence of the nature of the alcohol on their morphology and size but with a more drastic difference [57–59]. Indeed, where

sponge-like Ru agglomerates of 80–100 nm in size were observed with methanol, no big agglomerates were detected with propanol and heptanol. The morphology of the methanol-stabilized Ru nanoparticles was clearly polycrystalline with individual crystallites of a few nanometers [57]. This morphology was explained by a weak stabilizing effect of methanol that resulted in the aggregation of small individual Ru nanoparticles. In the contrary, the propanol- and heptanol-stabilized Ru nanomaterials were found to contain monocrystalline nanoparticles of ca. 5 and 3 nm in size, respectively [58, 59]. Here, the Rh nanoparticles appear all under the form of large polycrystalline objects with a similar size. However, the fact that propanol- and heptanol-stabilized Rh appears under the form of more regular in size assemblies compared to methanol-stabilized nanoparticles can be explained by higher stabilizing properties when the alkyl chain length of the alcohol increases as the result of more steric hindrance at the nanoparticle surface. Additionally, the similar size observed for both propanol- and heptanol-stabilized

Rh nanoparticles indicates that a chain length difference between three and seven carbon atoms does not have a significant influence on the morphology of the Rh nanoparticles. Remarkably, the sponge-like character of the obtained Rh nanoparticles is highly interesting because it may offer a high active surface for catalysis. In addition, alcohols are expected to be weak coordinating molecules at metal surface and not limit too much the catalytic reactivity. HRTEM images of the Rh nanoparticles synthesized in the presence of hexadecylamine showed dispersed nanoparticles of mean size in the range 5–10 nm exhibiting a sphere-like morphology. This result suggests that the long alkyl chain of the hexadecylamine present at the surface of Rh nanoparticles limited their aggregation and let to obtain a more homogeneous dispersion.

These Rh nanoparticles have been also characterized by powder X-ray diffraction as illustrated in Fig. 2. The three Rh nanomaterials prepared with alcohols showed four broad diffraction peaks at $2\theta = 41.07°, 47.41°, 70.17°$ and $84.37°$ (JCPDS Card
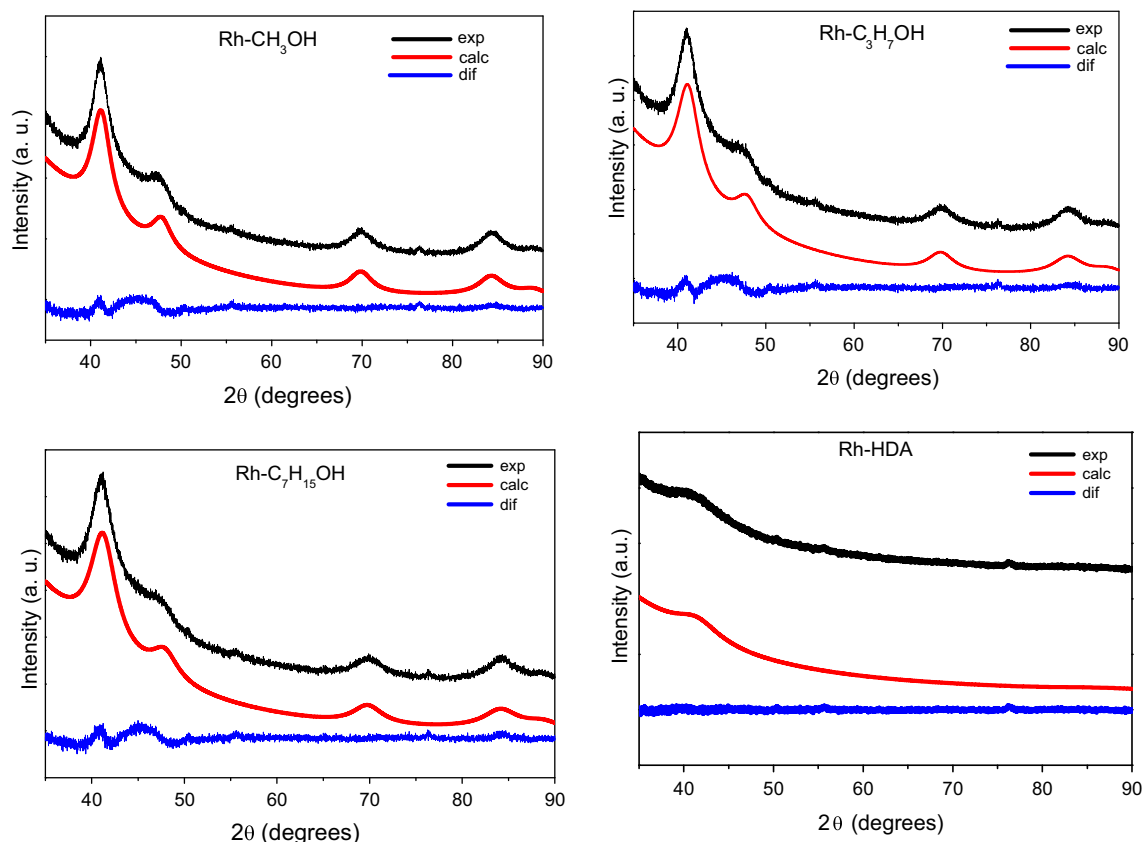

Figure 2 XRD patterns of Rh-methanol, Rh-propanol, Rh-heptanol and Rh-hexadecylamine/THF nanoparticles synthesized from Rh(η^3-C$_3$H$_5$)$_3$ under dihydrogen atmosphere.

Table 2 Crystallite size and lattice constant of Rh nanoparticles synthesized in alcohols calculated by a double-Voigt approach (LVol-IB) implemented in TOPAS V5 by a Rietveld fitting

Sample	Crystallite size (nm)	Lattice constant, a (nm)	RWP
Rh-CH$_3$OH	2.348 ± 0.019	3.8171 (10)	3.53
Rh-C$_3$H$_8$	1.959 ± 0.017	3.8221 (12)	3.39
Rh-C$_7$H$_{16}$	1.786 ± 0.015	3.8274 (13)	3.39
Rh-HDA	0.991 ± 0.019	3.833 (19)	2.32
Rh bulk	–	3.7957	–

No. 65-2866) in good agreement with single face-centered cubic structure, as expected for rhodium. There is no significant shift in the peak position due to the presence of CH$_3$–OH, C$_3$H$_7$–OH or C$_7$H$_{15}$–OH. Rh-hexadecylamine nanomaterial showed the same four diffraction peaks of fcc crystal structure; however, these peaks depict very low intensity indicating a very poor crystalline character. The crystallite size and lattice constant of Rh nanoparticles calculated by a double-Voigt approach (LVol-IB) implemented in TOPAS V5 and lattice constant of Rh nanoparticles calculated by a Rietveld fitting are shown in Table 2 [60, 61]. Additionally, structural parameters by Rietveld refinement are also shown in Table 3. These results indicate that the crystallite size of the Rh nanoparticles decreases as a function of the alkyl chain length of the alcohol from 2.3 nm for methanol to 1.7 nm for heptanol, as shown in Fig. 3. This tendency has been also observed for the Ru nanoparticles synthesized in the presence of methanol, n-propanol, isopropanol and pentanol [58]. From these data we can conclude that heptanol (1.7 nm) and propanol (1.8 nm) favor the stabilization of Rh crystallites of similar size and smaller than methanol (2.3 nm). Nevertheless, whatever the alkyl chain length, aggregation of crystallites into large assemblies of nanoparticles takes place giving rise to sponge-like big agglomerates.

Magnetic measurements

An important effect of nanostructuring metals by the synthesis of metal nanoparticles is the variation of their electronic structure through surface effects, which becomes increasingly important with reducing particle size [62, 63]. In this sense, magnetic measurements were taken to establish if the nanoscale character of the Rh nanoparticles produces a deviation from the characteristic paramagnetic response of bulk metallic Rh. Magnetization M curves as a function of external field H are shown in Fig. 4a for Rh-

CH$_3$OH, Rh-C$_3$H$_7$OH and Rh-C$_7$H$_{15}$OH nanomaterials. An unexpected ferromagnetic character at room temperature for the Rh nanoparticles is evidenced by the coercive field (H_c) of the M–H curves, as illustrated in Fig. 4b, for which H_c values between 16 and 29 Oe were recorded. In addition, the noticeable linear portion of each M–H curve for $H > 7000$ Oe (and $H < -7000$ Oe) is indicative of a paramagnetic response overlapped with the ferromagnetic behavior. In contrast, the magnetic response of Rh-HDA nanoparticles (Fig. 5a) reflects a predominant diamagnetic contribution coming from the sample holder. Subsequent subtraction of this instrument response reveals the typical ferromagnetic M–H plot of Fig. 5b, for which a very weak magnetization saturation of 0.00147 emu/g is manifested. The appearance of a magnetic moment for Rh nanoparticles with fcc crystal structure can be explained by a nanostructuring effect on their electronic structure, in particular, on the possibility to produce narrow 4d bands at the Fermi level E_F as a result of lattice expansions. These lattice variations were also observed in XRD results described in the previous section (see Table 2). Changes in the local symmetry due to surface defects (like twin boundaries) can also produce variations of the electronic structure of metallic nanoparticles. Narrow 4d bands favor the enhancement of density of states at the Fermi level $N(E_F)$, which in turn promotes the fulfilling of the Stoner criterion of magnetism $N(E_F)I > 1$, where I corresponds to the Stoner parameter. As I is considered as a constant of the material ($I = 0.40$ for metallic Rh [64]), the modulation of $N(E_F)$ is an effective way for promoting the development of magnetic moment in transition metal nanoparticles with 4d levels. Ferromagnetic ordering for our Rh nanoparticles stems from inner atoms where fcc structure is preserved, whereas the paramagnetic response can be ascribed to surface atoms, for which broken bonds or crystal symmetry variation is able to inhibit the exchange coupling between magnetic

Table 3 Structural parameters by Rietveld refinement

Model	Fm-3m				
Sample	Rh-methanol	Rh-heptanol	Rh-propanol	Rh-hexadecylamine	Rh bulk
Lattice parameter, a (Å)	3.8171	3.8274	3.8221	3.8330	3.7957
Cell volume (Å^3)	55.62	56.07	55.83	56.30	54.6860
R-factors (%)					
R_p	2.86	2.73	2.74	1.78	
R_{wp}	3.53	3.39	3.39	2.32	
R_{exp}	2.17	2.22	2.19	2.08	
R_{Bragg}	0.240	0.208	0.200	0.057	
χ^2	1.63	1.53	1.55	1.12	
Crystallite size (nm)	2.348	1.786	1.959	0.991	

Atomic position	x	y	z	x	y	z	x	y	z	x	y	z	x	y	z
Rh	0.0000	0.0000	0.0000	0.0000	0.0000	0.0000	0.0000	0.0000	0.0000	0.0000	0.0000	0.00000	0.0000	0.0000	0.0000

Figure 3 General representation of Rietveld analysis of Rh-methanol, Rh-propanol and Rh-heptanol nanoparticles.
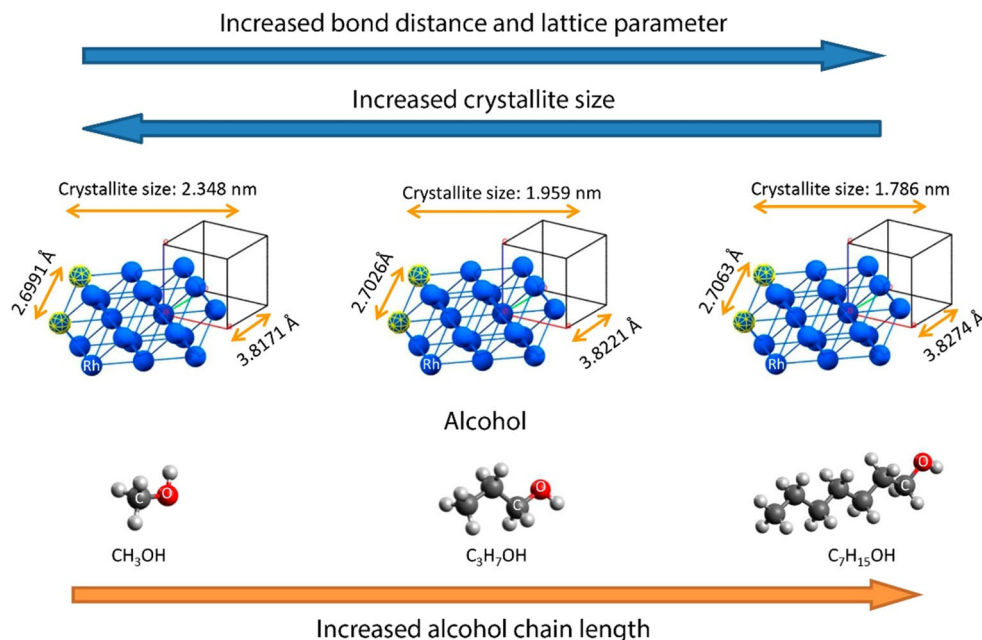

moments. According to Table 2, crystallite size of Rh nanoparticles is well below 10 nm, which implies that surface atoms represent a significant portion (around 20%) of atoms as seen in Table 2. The Rh-hexadecylamine nanoparticles possess the largest cell parameter, which promotes the enhancement of the exchange coupling interaction between neighboring magnetic moments of Rh atoms, thus facilitating the development of ferromagnetic ordering without paramagnetic contribution.

As previously described in the Experimental section, the paramagnetic and ferromagnetic contributions can be separated by fitting experimental data with Eq. (4). Figure 6 presents the paramagnetic and ferromagnetic contributions to the $M–H$ curve for Rh-$C_7H_{15}OH$ nanoparticles by using $M_0 = 3.98$ emu/g and $J = ½$. This value of J is justified for $3d$ and $4d$ elements because their angular moment L is quenched, and thus, $J = S$. The ferromagnetic curve exhibits a saturation $M_{ferr} = 0.01$ emu/g, and from the total saturation magnetization 3.99 emu/g, an effective magnetic moment of 0.073 μ_B per Rh atom is estimated. This value of magnetic moment per atom is similar to that observed for Pd nanoparticles (0.17 μ_B) with average size of 2.4 nm [65]. The estimated magnetic moment per Rh atom for the remaining ensembles of nanoparticles is 0.099 μ_B for Rh-CH_3OH and 0.036 μ_B for Rh-C_3H_7OH.

Surface area determination and activities on ORR

The electrochemical activities toward ORR of the rhodium nanoparticles here above described were initially studied by cyclic voltammetry. Cyclic voltammograms of the electrocatalysts for Rh-CH_3OH/C, Rh-C_3H_7OH/C and Rh-$C_7H_{15}OH$/C were recorded in 0.5 M H_2SO_4 solution with a scan rate of 20 mV s^{-1}, and the results are shown in Fig. 7a–c. It is well known that efficiency of nanoparticle stabilization afforded by a ligand system depends on the surface coverage, which in turn depends on the relative quantity and/or nature of the ligand initially introduced for the synthesis, i.e., strength of the metal–ligand interaction. Thus, for comparison purpose, the electrochemical performance of Rh-$C_{16}H_{33}NH_2$ (HDA)/C nanostructures was also measured as shown in Fig. 7d. Like platinum in H_2SO_4, the solubility of Rh species is potential dependent; thus, it is expected that Rh catalysts accelerate the oxidation of carbon and Rh sintering according to the following reactions [25, 66, 67].

$$C + 2H_2O \leftrightarrow CO_2 + 4H^+ + 4e^- \quad E^0 = 0.207\,V \quad (5)$$

or

$$C + H_2O \leftrightarrow H_2 + CO \quad (6)$$
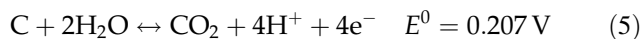
During this process, CO may poison the Rh catalysts; either CO_2 or CO formed during the carbon
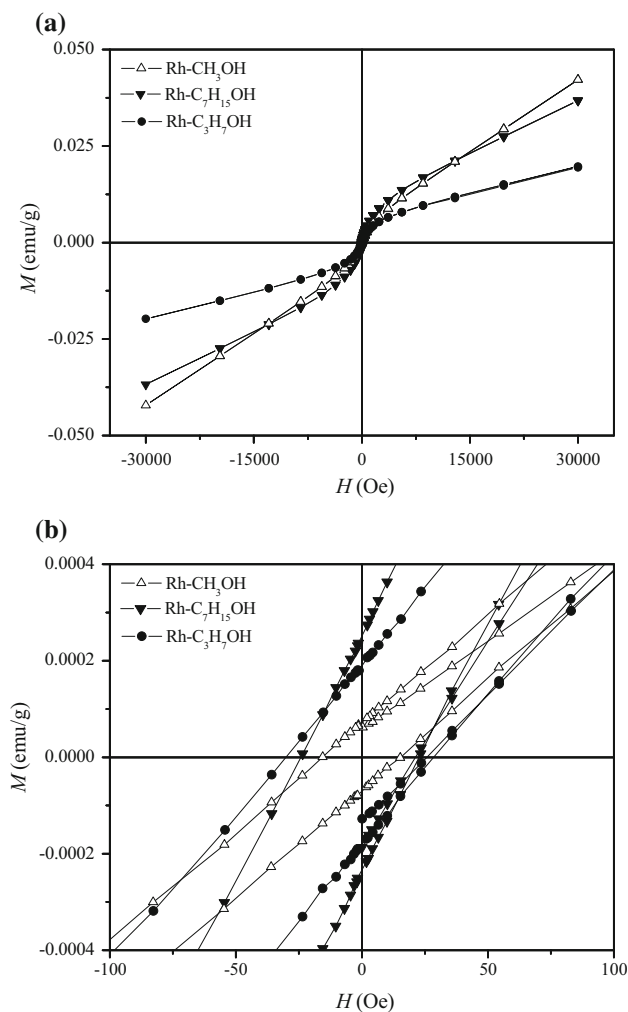
(a)

(b)

Figure 4 **a** *M–H* curves for Rh-methanol, Rh-heptanol and Rh-propanol nanoparticles, **b** enlarged sections of the *M–H* plot showing the coercive field for each ensemble of Rh nanoparticles.
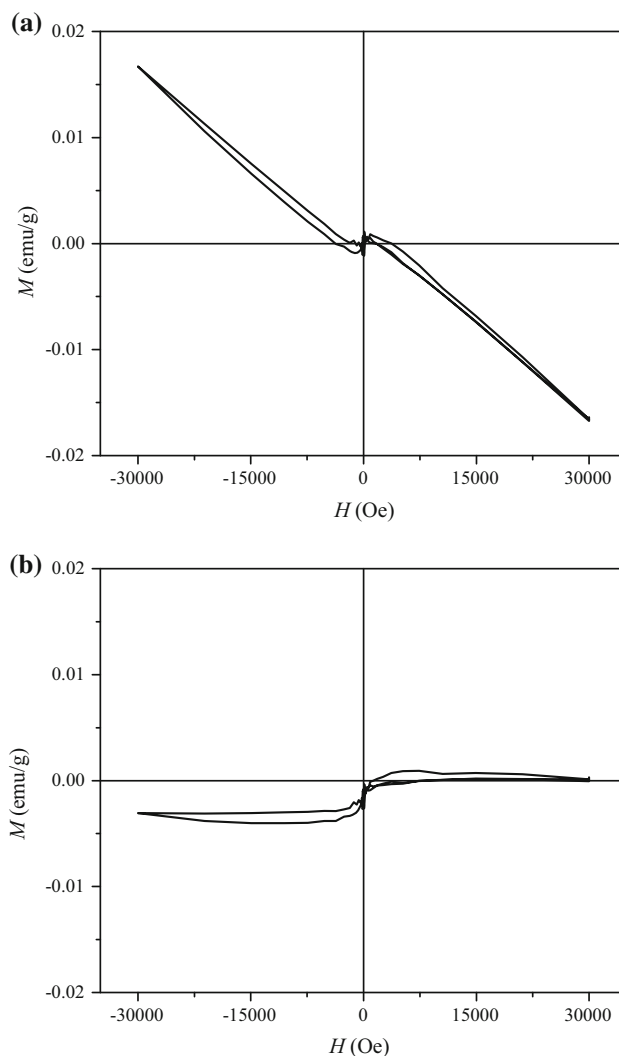
(a)

(b)

Figure 5 *M–H* curves for Rh-HDA nanostructures showing **a** the predominant diamagnetic instrumental contribution and **b** ferromagnetic behavior manifested after subtraction of instrument contribution.

oxidation will thus decrease the amount of carbon available for Rh loading, which makes the Rh nanoparticles to fall off the carbon support and finally decreases the electrochemical surface area. Under these considerations, the Rh dissolution/re-deposition is considered as the main mechanism, and to guarantee the electrode stabilization, materials were recorded to the activation process during at 15 potential cycles.

All the alcohol-stabilized Rh nanomaterials start to stabilize after three potential cycles, showing small capacitive currents. The typical sharp peaks associated with hydrogen adsorption–desorption are seen in the potential range from -0.0814 to $+0.1192$, -0.0586 to $+0.331$ and -0.054 to $+0.224$ V (SHE),

using CH_3OH, $C_3H_7–OH$ and $C_7H_{15}–OH$ as a stabilizer agent, respectively. On the other hand, the oxygen region was obtained at $+1.030$ to $+1.197$, $+1.14$ to $+1.40$ and $+1.093$ to $+1.200$ V (SHE) for the same order of catalysts. The peak at 0.718 V (SHE) represents the oxygen adsorption at the rhodium surface, which is reduced in the backward scan at 0.323 V_{SHE}. The changes for the hydrogen adsorption–desorption peaks and double-layer charging region appeared to be higher with the increasing of the chain length as observed with the shape or intensity of the voltammograms. In contrast, Rh-$C_{16}H_{33}NH_2$ catalyst displays a strongly quasi-irreversible behavior without clear peaks in the
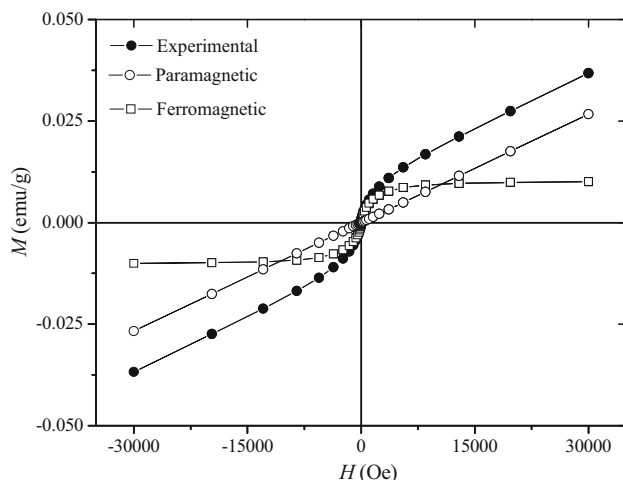
Figure 6 Separated ferromagnetic–paramagnetic contribution for Rh-$C_7H_{15}OH$ nanoparticles.

oxidation–reduction process. It has been previously demonstrated that the nature and amount of ligand can be tuned to obtain active metal particles [41]. Here, it is seen that the coordination of amino groups on the surface of Rh nanoparticles interferes with the electron transfer behavior of the Rh particles, thus affecting the amount of adsorbed hydrogen.

One of the most important objectives during electrocatalyst evaluation is the determination of electrochemical surface area (ECSA) which can be up to 10^3 times greater in comparison with the geometric area. Different methods for ECSA calculation have been previously reported highlighting advantages and limitations [66, 67]. In this study the electrode surface has been characterized to determine ECSA using the traditional hydrogen adsorption–desorption region and the following equation [25, 68].

$$\text{ECSA}\left[\frac{m^2}{g}\right] = \frac{Q_H}{(Q_{Rh})(m_{Rh})(10)} \qquad (7)$$

Q_H (µC cm^{-2}) represents the average charge from the integration of adsorption–desorption peaks in the so-called hydrogen region, i.e., $\frac{Q_{ads}+Q_{des}}{2}$, Q_{Rh} is the specific amount of electricity corresponding to the full coverage of the Rh by one monolayer of oxygen (the accepted values of Q_{Rh} are 221 and 256 (µC cm^{-2}), [25, 66, 69, 70]), and m_{Rh} (mg cm$^{-2}_{electrode}$) is the rhodium loading on the working surface electrode. Q_H was calculated by integrating voltammetric curves in the hydrogen region before subtracting the charge associated to double-layer capacitive process in the hydrogen adsorption region. ECSA

calculations of the as-prepared Rh samples evaluated in this work are shown in Table 4. The results indicate that when a R–OH ligand is used to stabilize the Rh nanoparticles, a long chain length is required to obtain similar ECSA than that observed with the hexadecylamine ($C_{16}H_{33}NH_2$) ligand. The active surface area displays a behavior in the following order Rh-$C_7H_{15}OH$/C > Rh-$C_{16}H_{33}NH_2$/C > Rh-C_3H_7OH/C > Rh-CH_3OH/C; in other words, the electroactivity of the Rh nanoparticles seems to be higher with increasing of the chain length, which in turn enhances van der Waals interactions between R–OH–Rh–OH–R chains and limits nanostructure agglomeration.

Rotating disk electrode measurements were taken to eliminate the mass transport effects. The electrocatalytic activity of the Rh stabilized electrodes toward the ORR was analyzed by polarization curves at different rotation speeds (ω = 100–1600 rpm) with a scan rate 5 mV s^{-1}, and the results are shown in Fig. 8a–d. The polarization curves displayed traditional potential regions: the diffusion-limiting current region below 0.5 V$_{SHE}$ and the mixed kinetic–diffusion control between 0.5 and 1.0 V$_{SHE}$. In general, as expected, diffusion-limited current density increases gradually with the rotation speed. The increase in oxygen diffusion and the lower effect of mass transports at higher rotation rates have been well documented due to increase in the reduction current density. The diffusion-limiting current region below 0.4 V$_{SHE}$ in O$_2$ saturated electrolyte indicates that Rh-$C_7H_{15}OH$/C and Rh-$C_{16}H_{33}NH_2$/C catalysts have high electrocatalytic activity for ORR.

The kinetic parameters for oxygen reduction such as kinetic current density, exchange current density and Tafel slopes are important indicators to evaluate the ORR performance and were determined by plotting Koutecky–Levich (K–L) equation ($\frac{1}{\sqrt{\omega}}$ versus $\frac{1}{j}$) at five potentials different potentials in the range from 0.1 to 0.7 V$_{SHE}$. The overlapped and parallel lines in the K–L plots (see insets in Fig. 8a–d) adjusted well with electron transfer number of four per oxygen molecule during ORR process, with the traditional one-step pathway O$_2$ + 4H$^+$ + 4e$^-$ $\leftrightarrow$ 2H$_2$O; it was noteworthy to mention that the stabilizer nature and length of chain do not change the typical ORR mechanism.

In summary, the ORR polarization curves and the kinetic parameters indicate that Rh-$C_{16}H_{33}NH_2$/C
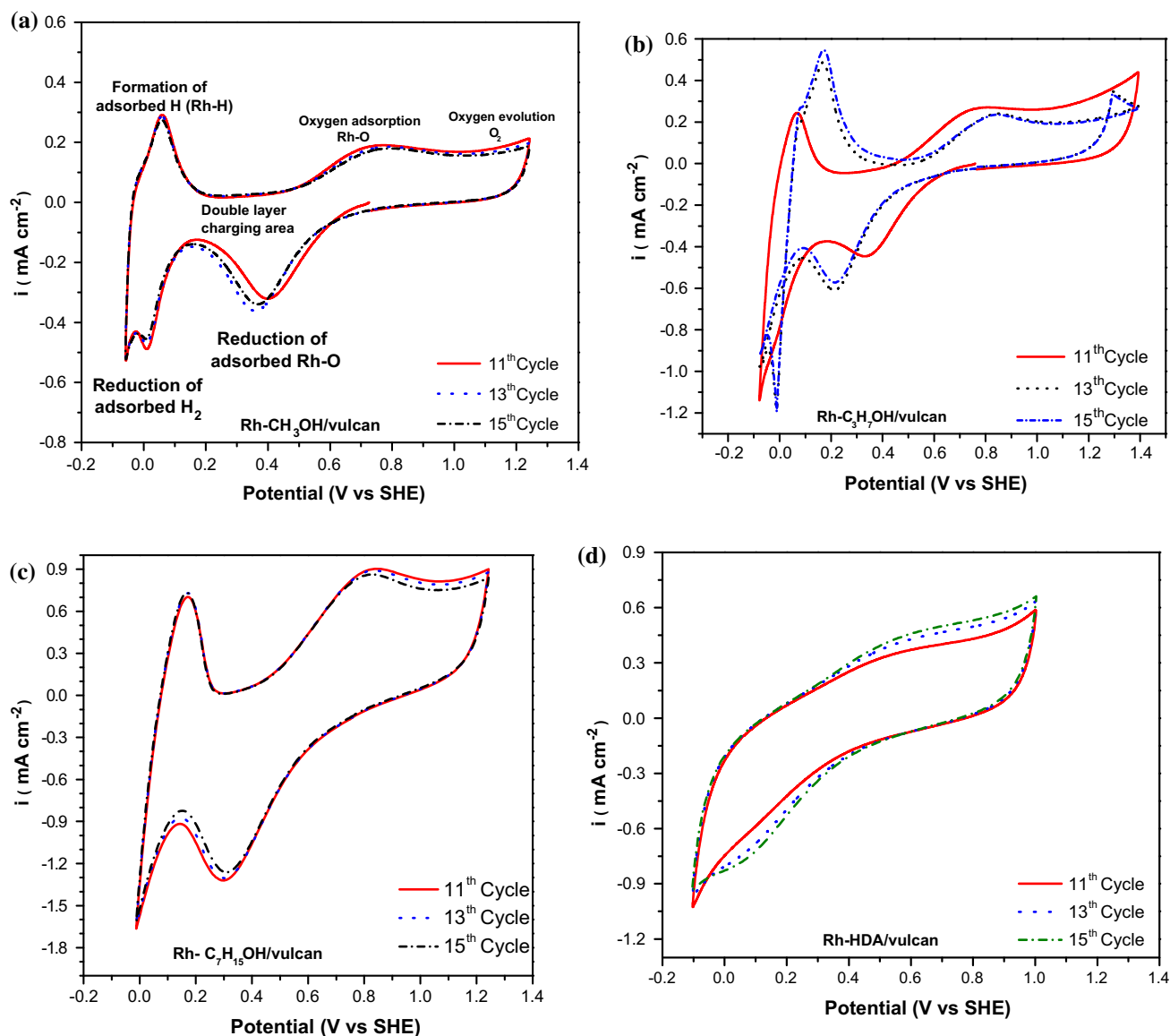
Figure 7 Cyclic voltammograms for Rh nanoparticles stabilized with **a** methanol, **b** propanol, **c** heptanol and **d** hexadecylamine (HDA) in 0.5 H$_2$SO$_4$, scan rate 20 mV s^{-1}.

Table 4 Comparative performance data of electrocatalysts with different stabilizers and Rh/C reported from Ref. [68]

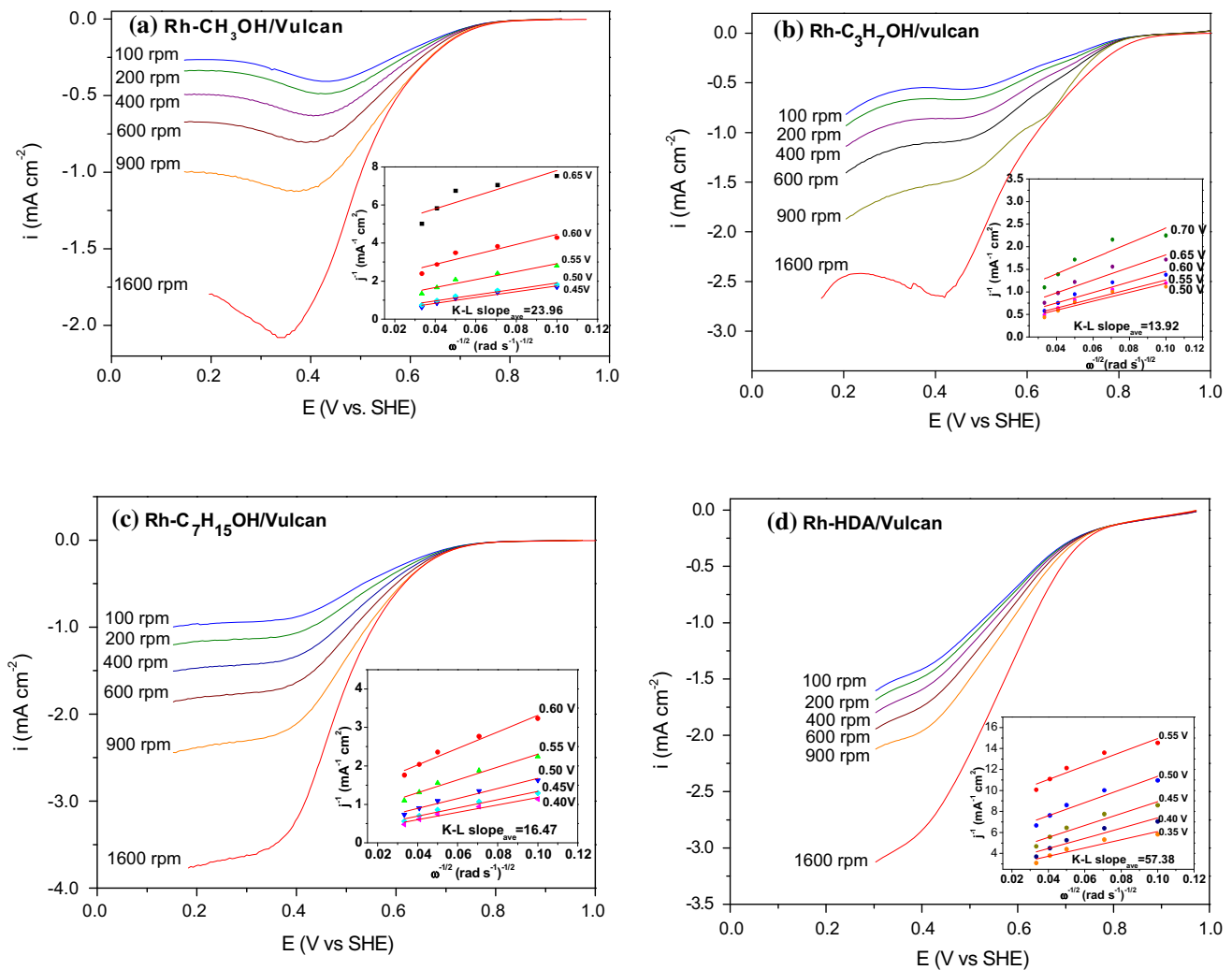| Electrode (20 wt% metal)	Rh loading (mg cm^{-2})	Q$_H$ (μC cm^{-2})	ECSA m^2 g^{-1}	Tafel slope (mV decade^{-1})	i_k (@ 0.55 V) (mA cm^{-2})	Log i_o (mA cm^{-2})
Rh-CH$_3$OH/C	0.0072	47.9	3.10	− 176.5	0.032 (0.135)	− 4.6
Rh-C$_3$H$_7$OH/C		162.5	10.21	− 128.6	0.210 (0.260)	− 4.2
Rh-C$_7$H$_{15}$OH/C		208.9	13.13	− 167.3	0.010 (0.41)	− 4.0
Rh-C$_{16}$H$_{33}$NH$_2$/C		178.1	11.24	− 244.4	0.040 (0.49)	− 4.0
Rh/C [60]	0.0110	–	25.6	− 122.3	1.870	− 2.6

Figure 8 LSV curves of Rh electrocatalysts at different rotating rates with their corresponding K–L plots using **a** methanol, **b** propanol **c** heptanol and **d** hexadecylamine in O_2-saturated 0.5 M H_2SO_4.

and Rh-C_7H_{15}OH/C electrode materials display similar catalytic activities and that they are higher than those observed for CH_3OH and C_3H_7OH-stabilized Rh nanoparticles.

Conclusions

The synthesis of Rh nanoparticles was successfully carried out by hydrogenation treatment of Rh(η^3-C_3H_5)$_3$ as metal source in methanol, propanol and heptanol as reaction media and in the absence of any other stabilizer. A comparison of the results obtained depending on the alkyl chain length of the alcohol used allowed us to get information on the stabilization ability of these alcohols at Rh particle surface

and on their influence on the electrocatalytic performance in ORR. Whatever the alkyl chain length of the alcohol, aggregation of Rh crystallites into large and sponge-like assemblies was observed by transmission electron microscopy. Powder X-ray analysis indicated that heptanol and propanol favored the stabilization of Rh crystallites of similar size (1.7 and 1.8 nm, respectively) but smaller than methanol (2.3 nm), all with the fcc crystal structure and lattice expansions. Magnetic measurements revealed an unexpected ferromagnetic character at room temperature. The appearance of a magnetic moment for Rh nanoparticles with fcc crystal structure is attributed to the nanostructuring effect on their electronic structure, in particular, on the possibility to produce narrow 4d bands at the Fermi level E_F as a result of

lattice expansions. Magnetic moment per Rh atom was estimated to be 0.099 μ_B for Rh-CH$_3$OH, 0.036 μ_B for Rh-C$_3$H$_7$OH and 0.073 μ_B for Rh-C$_7$H$_{15}$OH.

Electrocatalysis studies indicated that OH$^-$ groups do not change the typical ORR mechanism which can be explained by the weak stabilizing character of the alcohols. However, it appeared that a long chain length favors greatly the electroactivity on ORR. Interestingly, a ferromagnetic ordering at room temperature appeared, as the result of the nanostructure character of the Rh particles, for which a maximum magnetic moment of 0.099 μ_B per Rh atom was estimated for the Rh nanoparticles synthesized with methanol.

Acknowledgements

References

[1] Hasa B, Kalamaras E, Papaioannou EI, Vakros J, Sygello L, Katsaounis A (2015) Effect of TiO$_2$ loading on Pt–Ru catalysts during alcohol electrooxidation. Electrochim Acta 179:578–587

[2] Hamnett A, Vielstich W, Lamm A, Gasteiger HA (2003) Handbook of fuel cells: fundamentals, technology and applications. Wiley, Chichester

[3] Zhang J (2008) PEM fuel cell electrocatalysts and catalyst layers. Springer, Berlin

[4] Banham D, Ye S, Pei K, Ozaki JI, Kishimoto T, Imashir Y (2015) A review of the stability and durability of non-precious metal catalysts for the oxygen reduction reaction in proton exchange membrane fuel cells. J Power Sour 285:334–348

[5] Gewirth AA, Thorum MS (2010) Electroreduction of dioxygen for fuel-cell applications: materials and challenges. Inorg Chem 49:3557–3566

[6] Jacinto MJ, Kiyohara PK, Masunaga SH, Jardim RF, Rossi LM (2008) Recoverable rhodium nanoparticles: synthesis, characterization and catalytic performance in hydrogenation reactions. Appl Catal A Gen 338:52–57

[7] Schmid G (2012) Nanoparticles: from theory to application, 2nd edn. Wiley-VCH Verlag, Weinheim

[8] Chen LY, Fujita T, Ding Y, Chen MW (2010) A three-dimensional gold-decorated nanoporous copper core-shell composite for electrocatalysis and nonenzymatic biosensing. Adv Funct Mater 20:2279–2285

[9] Tao AR, Habas S, Yang P (2008) Shape control of coloidal metal nanocrystals. Small 4:310–325

[10] Sau TK, Rogach AL (2010) Nonspherical noble metal nanoparticles: colloid-chemical synthesis and morphology control. Adv Mater 22:1781–1804

[11] Davis SA, Breulmann M, Rhodes KH, Zhang B, Mann S (2001) Template-directed assembly using nanoparticle building blocks: a nanotectonic approach to organized materials. Chem Mater 13:3218–3226

[12] Li D, Cui Y, Wang K, He Q, Yan X, Li J (2007) Thermosensitive nanostructures comprising gold nanoparticles grafted with block copolymers. Adv Funct Mater 17:3134–3140

[13] Cai B, Dianat A, Hübner R, Liu W, Wen D, Benad A, Sonntag L, Gemming T, Cuniberti G, Eychmüller A (2017) Multimetallic hierarchical aerogels: shape engineering of the building blocks for efficient electrocatalysis. Adv Mater 29:1605254

[14] Le Rhun V, Garnier E, Pronier S, Alonso-Vante N (2000) Electrocatalysis on nanoscale ruthenium-based material manufactured by carbonyl decomposition. Electrochem Commun 2:475–479

[15] Bron M, Bogdanoff P, Fiechter S, Hilgendorff M, Radnik J, Dorbandt I, Schulenburg H, Tributsch H (2001) Carbon supported catalysts for oxygen reduction in acidic media prepared by thermolysis of Ru$_3$(CO)$_{12}$. J Electroanal Chem 517:85–94

[16] Castellanos RH, Borja-Arco E, Altamirano-Gutiérrez A, Ortega-Borges R, Meas Y, Jiménez-Sandoval O (2005) Electrocatalytic properties of novel ruthenium-based compounds for the oxygen reduction reaction in 0.5 M H$_2$SO$_4$: effects of the synthesis atmosphere and temperature. J New Mater Electrochem Syst 8:69–75

[17] Guyonnet Bilé E, Sassine R, Denicourt-Nowicki A, Launay F, Roucoux A (2011) New ammonium surfactant-stabilized rhodium(0) colloidal suspensions: influence of novel

counter-anions on physico-chemical and catalytic properties. Dalton Trans 40:6524–6531

[18] Trang Thanh Chau N, Menuel S, Colombel-Rouen S, Guerrero M, Monflier E, Philippot K, Denicourt-Nowicki A, Roucoux A (2016) Active hydrogenation Rh nanocatalysts protected by new self-assembled supramolecular complexes of cyclodextrins and surfactants in water. RSC Adv 6:108125–108131

[19] Gacem N, Diao P (2013) Effect of solvent polarity on the assembly behavior pf PVP coated rhodium nanoparticles. Colloids Surf A Physicochem Eng Asp 417:32–38

[20] Long NV, Chien ND, Hirata H, Matsubara T, Ohtaki M, Nogami M (2011) Highly monodisperse cubic and octahedral rhodium nanocrystals: their evolutions from sharp polyhedrons into branched nanostructures and surface-enhanced Raman scattering. J Cryst Growth 320:78–89

[21] Marín-Almazo M, Ascencio JA, Pérez-Álvarez M, Gutiérrez-Wing C, José-Yacaman M (2005) Synthesis and characterization of rhodium nanoparticles using HREM techniques. Microchem J 81:133–138

[22] Suo Y, Hsing I-M (2011) Highly active rhodium/carbon nanocatalysts for ethanol oxidation in alkaline medium. J Power Sour 196:7945–7950

[23] Durap F, Zahmakiran M, Özkar S (2009) Water soluble laurate-stabilized rhodium(0) nanoclusters catalyst with unprecedented catalytic lifetime in the hydrolytic dehydrogenation of ammonia-borane. Appl Catal A 369:53–59

[24] Karschin A, Katsounaros I, Klemm SO, Meier JC, Mayrhofer KJJ (2012) Degradation of polycrystalline rhodium and rhodium nanoparticles. Electrochim Acta 70:355–359

[25] Tzorbatzoglou F, Brouzgou A, Tsiakaras P (2015) Electrocatalytic activity of Vulcan-XC-72 supported Pd, Rh and PdxRhy toward HOR and ORR. Appl Catal B 174–175:203–211

[26] Lin C, Wu G, Li H, Geng Y, Xie G, Yang J, Liu B, Jin J (2017) Rh nanoparticles supported on ultrathin carbon nanosheets for high-performance oxygen reduction reaction and catalytic hydrogenation. Nanoscale 9:1834–1839

[27] Yao L, Zhao J, Lee J-M (2017) Small size Rh nanoparticles in micelle nanostructure by ionic liquid/CTAB for acceptorless dehydrogenation of alcohols only in pure water. ACS Sustain Chem Eng 5:2056–2060

[28] Hoefelmeyer JD, Liu H, Somorjai GA, Tilley TD (2007) Reverse micelle synthesis of rhodium nanoparticles. J Colloid Interface Sci 309:86–93

[29] Xie S, Zhang H, Lu N, Jin M, Wang J, Kim MJ, Xie Z, Xia Y (2013) Synthesis of rhodium concave tetrahedrons by collectively manipulating the reduction kinetics, facet-selective capping, and surface diffusion. Nano Lett 13:6262–6268

[30] Zahmakiran M, Özcar S (2009) Dimethylammonium hexanoate stabilized rhodium(0) nanoclusters identified as true heterogeneous catalysts with the highest observed activity in the dehydrogenation of dimethylamine-borane. Inorg Chem 48:8955–8964

[31] Ayvali T, Zahmakiran M, Özcar S (2011) One-pot synthesis of colloidally robust rhodium(0) nanoparticles and their catalytic activity in the dehydrogenation of ammonia-borane for chemical hydrogen storage. Dalton Trans 40:3584–3591

[32] Li Y, Li N, Yanagisawa K, Ding X, Li X, Wei Y, Yan X (2013) Spherical Rh17S15@C and Rh@C core-shell nanocomposites: synthesis, growth mechanism and methanol tolerance in oxygen reduction reaction. Chem Eng J 228:45–53

[33] Uribe-Godínez J, García-Montalvo V, Jiménez-Sandoval O (2013) Development of Ir-based and Rh-based catalyst electrodes for PEM fuel cell applications. Int J Hydrog Energy 38:7680–7683

[34] Khosravian H, Liang Z, Uhl A, Trenary M, Meyer R (2012) Controlled Synthesis of Rh nanoparticles on TiO2(110) via Rh(CO)2(acac). J Phys Chem C 116:11987–11993

[35] Axet MR, Castillón S, Claver C, Philippot K, Lecante P, Chaudret B (2008) Chiral diphosphite-modified rhodium(0) nanoparticles: catalyst reservoir for styrene hydroformylation. Eur J Inorg Chem 22:3460–3466

[36] Ramírez-Meneses E, Philippot K, Chaudret B (2015) Influencia del medio de reacción en la estabilización de nanoestructuras de Rodio. Ingeniería Investigación y Tecnología 16:225–237

[37] Ibrahim M, Poreddy R, Philippot K, Riisager A, Garcia-Suarez EJ (2016) Chemoselective hydrogenation of arenes by PVP supported Rh nanoparticles. Dalton Trans 45:19368–19373

[38] Zhang J, Ibrahim M, Collière V, Asakura H, Tanaka T, Teramura K, Philippot K, Yang N (2016) Rh nanoparticles with NiOx surface decoration for selective hydrogenolysis of C–O bond over arene hydrogenation. J Mol Catal A Chem 422:188–197

[39] Ibrahim M, Garcia MAS, Vono LLR, Guerrero M, Lecante P, Rossi LM, Philippot K (2016) Polymer versus phosphine stabilized Rh nanoparticles as components of supported catalysts: implication in the hydrogenation of cyclohexene model molecule. Dalton Trans 45:17782–17791

[40] Karahan S, Zahmakiran M, Özkar S (2012) A facile one-step synthesis of polymer supported rhodium nanoparticles in organic medium and their catalytic performance in the dehydrogenation of ammonia-borane. Chem Commun 48:1180–1182

[41] Domínguez-Crespo MA, Ramírez-Meneses E, Montiel-Palma V, Torres Huerta AM, Dorantes Rosales H (2009)

Synthesis and electrochemical characterization of stabilized nickel nanoparticles. Int J Hydrog Energy 34:1664–1676

[42] Ramírez-Meneses E, Montiel-Palma V, Domínguez-Crespo MA, Izaguirre-López MG, Palacios-González E, Dorantes-Rosales H (2015) Shape-and size-controlled Ag nanoparticles stabilized by in situ generated secondary amines. J Alloys Compd 643:s51–s61

[43] Ramírez-Meneses E, Domínguez-Crespo MA, Montiel-Palma V, Chávez-Herrera VH, Gómez E, Hernández-Tapia G (2009) Electrochemical characterization of platinum nanoparticles stabilized by amines. J Alloys Compd 483:573–577

[44] Domínguez-Crespo MA, Ramírez-Meneses E, Torres-Huerta AM, Dorantes-Rosales H (2011) Effect of amine ligands on stabilization of Pt nanoparticles as electrode materials for electro-oxidation of methanol. J New Mater Electrochem Syst 14:1–10

[45] Domínguez-Crespo MA, Ramírez-Meneses E, Torres-Huerta AM, Garibay-Febles V, Philippot K (2012) Kinetics of hydrogen evolution reaction on stabilized Ni, Pt and Ni–Pt nanoparticles obtained by an organometallic approach. Int J Hydrog Energy 37:4798–4811

[46] Manzo-Robledo A, Costa Natália JS, Philippot K, Rossi Liane M, Ramírez-Meneses E, Guerrero-Ortega LPA, Ezquerra-Quiroga S (2015) Electro-oxidation of methanol in alkaline conditions using Pd–Ni nanoparticles prepared from organometallic precursors and supported on carbon Vulcan. J Nanoparticle Res 17:474

[47] Ramirez-Meneses E (2004) Synthèse et caractérisation de nanoparticules métalliques à base de rhodium, platine et palladium, stabilisées par des ligands. PhD thesis, Universite Paul Sabatier-Toulouse

[48] Hermann WA, Brauer G (2000) Synthetic methods of organometallic and inorganic chemistry (Hermann/Brauer): transition metals. Thieme Medical Publisher, Stuttgart

[49] Ibrahim M (2016) Rhodium based mono-and bi-metallic nanoparticles: synthesis, characterization and application in catalysis. PhD thesis, Université Paul Sabatier-Toulouse

[50] Coelho AA (2000) Whole-profile structure solution from powder diffraction data using simulated annealing. J Appl Cryst 33:899–908

[51] Lejaeghere K, Van Speybroeck V, Van Oost G, Cottenier S (2014) Error estimates for solid-state density-functional theory predictions: an overview by means of the ground-state elemental crystals. Crit Rev Solid State Mater Sci 39:1–24

[52] Durón S, Rivera-Noriega R, Nkeng P, Poillerat G, Solorza-Feria O (2004) Kinetic study of oxygen reduction on nanoparticles of ruthenium synthesized by pyrolysis of $Ru_3(CO)_{12}$. J Electroanal 566(2004):281–289

[53] Pleskov YV, Filinovskii VY (1976) The rotating disk electrode. Plenum Press, New York

[54] Hsueh K-L, Gonzalez ER, Srinivasan S (1983) Electrolyte effects on oxygen reduction kinetics at platinum: a rotating ring-disc electrode analysis. Electrochim Acta 28(1983):691–697

[55] Baysinger G, Berger LI, Goldberg RN, Kehiaian HV, Kuchitsu K, Rosenblatt G, Roth DL, Zwillinger D (2005) CRC handbook of chemistry and physics, 74th edn. CRC Press, Boca Raton FL

[56] Liu Y, Tang N, Wan X, Feng Q, Li M, Xu Q, Liu F, Du Y (2013) Realization of ferromagnetic graphene oxide with high magnetization by doping graphene oxide with nitrogen. Sci Rep 3:2566

[57] Vidoni O, Philippot K, Amiens C, Chaudret B, Balmes O, Malm J-O, Bovin J-O, Senocq F, Casanove M-J (1999) Novel, spongelike ruthenium particles of controllable size stabilized only by organic solvents. Angew Chem Int Ed 38:3736–3738

[58] Pelzer K, Vidoni O, Philippot K, Chaudret B, Collière V (2003) Organometallic synthesis of size-controlled poly-crystalline ruthenium nanoparticles in the presence of alcohols. Adv Funct Mater 13:118–126

[59] Pelzer K, Philippot K, Chaudret B (2003) Synthesis of monodisperse heptanol stabilized ruthenium nanoparticles. Evidence for the presence of surface hydrogen. Z Phys Chem 217:1539–1548

[60] Balzar D, Audebrand N, Daymond MR, Fitch A, Hewat A, Langford JI, Le Bail A, Louër D, Masson O, McCowan CN, Popa NC, Stephens PW, Toby BH (2004) Size-strain line-broadening analysis of the ceria round-robin sample. J Appl Cryst 37:911–924

[61] Balzar D (1999) International union of crystallography monographs on crystallography, vol 10. Oxford University Press, New York

[62] Lu A-H, Salabas EL, Schüth F (2007) Magnetic nanoparticles: synthesis, functionalization and application. Angew Chem Int Ed 46:1222–1244

[63] Singamaneni S, Bliznyuk VN, Binek C, Tsymbal EY (2011) Magnetic nanoparticles: recent advances in synthesis, self-assembly and applications. J Mater Chem 21:16819–16845

[64] Getzlaff M (2008) Fundamentals of magnetism. Springer, Berlin

[65] Sampedro B, Crespo P, Hernando A, Litrán R, Sánchez López JC, López Cartes C, Fernandez A, Ramírez J, González Calbet J, Vallet M (2003) Ferromagnetism in fcc twinned 2.4 nm Size Pd nanoparticles. Phys Rev Lett 91:237203

[66] Trasatti S, Petrii OA (1991) Real surface area measurements in electrochemistry. Pure Appl Chem 63(1991):711–734

[67] Łukaszewski M, Soszko M, Czerwiński A (2016) Electrochemical methods of real surface area determination of noble metal electrodes—an overview. Int J Electrochem Sci 11:4442–4469

[68] Chi Linh D, Thy San P, Ngoc Phong N, Viet Quan T (2013) Properties of Pt/C nanoparticle catalysts synthesized by electroless deposition for proton exchange membrane fuel cell. Adv Nat Sci Nanosci Nanotechnol 4:035011

[69] Clavilier J, Wasberg M, Petit M, Klein LH (1994) Detailed analysis of the voltammetry of Rh(111) in perchloric acid solution. J Electroanal Chem 374:123–131

[70] Langkau T, Baltruschat H (1998) The rate of anion and hydrogen adsorption on Pt(111) and Rh(111). Electrochim Acta 44:909–918